11

Modeling of wake-vortex detection by a ground-based fiber LIDAR system

S. Brousmiche, L. Bricteux,
G. Winckelmans, B. Macq and P. Sobieski
Ecole Polytechnique de Louvain, Université catholique de Louvain
Belgium

1. Introduction

Due to its lift force, an aircraft releases large scale swirling flows in its wake. As these vortices can impact significantly the trajectory of a following aircraft, their study is of great importance for practical applications concerning safety in aircraft traffic management. A well-adapted system to detect them is the heterodyne Doppler LIDAR (Light Detection And Ranging). Moreover, fiber-based LIDAR are known for their higher flexibiliy and compacity despite that they are limited in pulse energy. However, to reach optimal performances, it is often needed to precisely model the whole measurement process including atmospheric effects such as the refractive turbulence. Some parameters have to be tuned depending on the application as, for example, the pulse energy and duration, the pulse repetition frequency or the telescope dimensions. Wake vortices detection and intensity estimation also require a good compromise between spatial resolution and velocity precision which also depends on the scanning configuration.
The aim of this chapter is twofold. On the one hand, it describes a complete simulation method to evaluate the performance of a Doppler LIDAR for aircraft wake vortices detection near the ground. The principal interest of the simulation presented here is to combine a LASER beam propagation method with fluid dynamics simulations. On the other hand, it proposes effective wind velocity map reconstruction algorithms. The performance of spectral and correlogram accumulation algorithms in the vicinity of wake vortices is analyzed. The effect of velocity gradients on the estimation error is thus addressed.
After introducing the wake vortex phenomenon and its detection using a heterodyne Doppler LIDAR , the section 2 will discuss the measurement simulation. The numerical simulation of the wake in ground effect is then detailled in section 3. The processing algorithms are finally explained in section 4.

1.1 Wake-vortex fundamentals

The lift force acting on an aircraft is due to the pressure difference between the lower side (pressure side) and the upper side (suction side) of its wing. As a result of this pressure difference, there is a spanwise flow at the edges of the wing from the pressure side to the suction side. This pressure difference forces the suction side streamlines to converge toward the center of the wing and the pressure side streamlines to diverge from it. This spanwise flow combined with the free-stream velocity produces a swirling motion of the air trailing downstream of the wing. Just behind the trailing edge, a vortex sheet is shed which rolls-up

rapidly within a few span lengths to form a pair of counter rotating vortices of equal strength. The circulation, Γ [m^2/s], of the velocity field [m/s], $\mathbf{u}$, for each vortex is a quantity of primary importance as it gives an image of the vortex strength. For a closed contour $\mathcal{C} = \partial\Omega$ enclosing a patch of vorticity defined by the field $\boldsymbol{\omega} = \nabla \times \mathbf{u}$,

$$\Gamma = \int_{\Omega} \boldsymbol{\omega} \cdot \mathbf{n}\, dS = \oint_{\mathcal{C}} \mathbf{u} \cdot \mathbf{dl}\,. \tag{1}$$

In the particular case of a vortex alone, it is natural to choose a circular integration contour $\mathcal{C}$ and since the velocity field has the form $\mathbf{u} = u_\theta(r)\,\widehat{\mathbf{e}}_\theta$ it follows that:

$$\Gamma(r) = 2\pi r\, u_\theta(r) \tag{2}$$

The velocity profile is thus closely related to the circulation profile. The circulation and the velocity tangential distribution are given by the following relations:

$$\Gamma(r) = \Gamma_0 \frac{r^2}{\left(r^2 + r_c^2\right)}\,, \tag{3}$$

$$u_\theta(r) = \frac{\Gamma(r)}{2\pi r}\,. \tag{4}$$

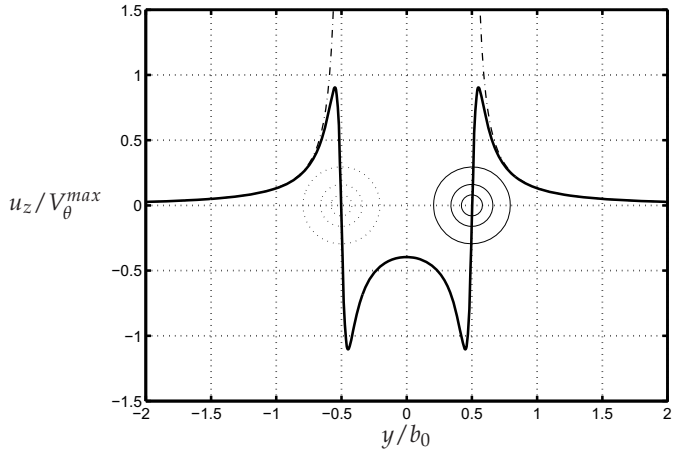

Fig. 1. Vertical velocity profile in the far wake of an aircraft. The dashed-dotted lines represent the potential velocity profile $V_\theta = \frac{\Gamma_0}{2\pi r}$. The curve is normalized by $V_\theta^{max} = \frac{\Gamma_0}{4\pi r_c}$ in the case of a low order algebraic model.

The parameters are Γ_0 [m$^{-2}/s$], the total circulation of the vortex and r_c [m], the radius of maximum induced tangential velocity. It is an indicator of the core size of a vortex; typically it amounts, after the initial roll-up phase, to $3-5\%$ of the wing span b. A typical velocity profile for a pair of vortices is illustrated in Fig. 1. A downwash velocity will alter the trajectory of an airplane passing between the two vortices. If it passes on one of the sides of the vortex pair, it will feel an upwash velocity. If the airplane enters in a vortex zone, a strong rolling moment

Leader aircraft max take-off weight	Follower aircraft (metric tons)	Separation Nautical miles	Time delay [s] Approach speed: $70m/s$
Heavy	Heavy ($\geq 136T$)	4	106
Heavy	Medium($< 136T$)	5	132
Heavy	Light ($\leq 7T$)	6	159
Medium	Light	5	132

Table 1. International Civil Aviation Organization (ICAO) aircraft separation distances to avoid wake vortex encounter, in nautical miles ($1\ NM = 1.852\ km$). For all other combinations, the separation is $3\ NM$. Table reproduced from Gerz et al. (2001).

will be applied to it. The momentum conservation allows to bind the initial circulation Γ_0 of an aircraft vortex pair to the lift force itself, equal to the weight of the aircraft:

$$L = Mg = \rho U b_0 \Gamma_0 , \tag{5}$$

where U [m/s] is the flight velocity and ρ is the fluid density. The circulation is thus proportional to the mass M of the aircraft and inversely proportional to its flight speed U. Typical values for the circulation range in $\Gamma_0 \approx 400 - 600\ \mathrm{m}^2/\mathrm{s}$ for heavy aircrafts. The length b_0 is the distance between the vortex cores; its value is approximately $b_0 = \frac{\pi}{4} b$ (assuming elliptical loading) with b the wingspan. The vortex spacing b_0 can be deduced following the lifting line theory (Prandtl, 1957). Wake vortices generated at take-off are very strong since the airplane evolves at low speed and is fully loaded. Aircraft wake vortices are also the source of the drag induced by the lift force acting on the aircraft: the so-called *induced drag*.

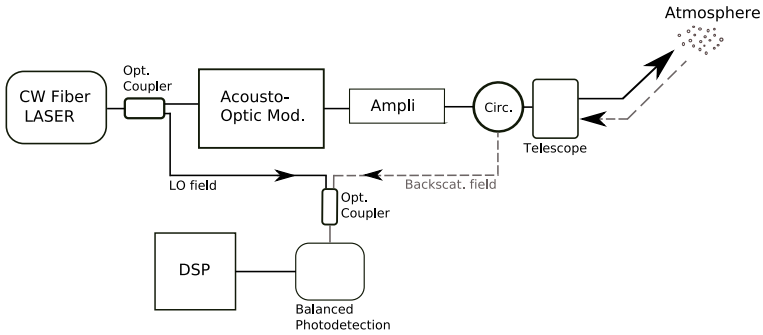

Fig. 2. Classical heterodyne Doppler LIDAR architecture based on a fiber LASER source.

1.2 Detection using a heterodyne Doppler LIDAR

A general architecture for a heterodyne Doppler LIDAR is given at Fig. 2. The heart of the system is a continuous LASER source producing a quasi-monochromatic optical wave. The $1.55\ \mu m$ fiber-based LASER sources are used as an alternative to classical sources due to their higher compacity and flexibility. Moreover, although the pulse energy is rather low (i.e. a few hundreds of microjoules), they are able to produce a higher pulse repetition frequency. When passing through the acousto-optic modulator, the wave is shifted in frequency and modulated

to produce a LASER pulse with a global Gaussian shape. The intermediate frequency is typically chosen around 70 MHz. The pulse duration has a duration varying from 100 ns to 1 μs depending on the spatial resolution needed. This pulse is then amplified and emitted through the atmosphere using a telescope. The telescope configuration is usually monostatic which means that the energy is sent and received through the same aperture. This requires however the use of a circulator. The monostatic configuration has less sensitivity to higher spatial scales of the atmospheric turbulence. As it propagates, the emitted beam is scattered by the aerosols particles. A portion of the backscattered energy is received at the telescope and is mixed with the local oscillator beam coming from the LASER source. A balanced photodetector produces the heterodyne current which oscillates around the intermediate frequency depending on the Doppler effect induced by the movement of the aerosol particles along the line-of-sight. The signal is then processed to estimate wind velocity maps, detect the wake vortices and estimate their circulation.

Most of the LIDAR systems used for wake-vortex detection are ground-based with a 2D scanning perpendicular to the runways as illustrated in Fig. 3. This allows to better discriminate the velocity signal due to the vortices from that due to the background turbulence, which is weaker. The angular resolution of the system is defined by the angular scanning velocity and the pulse repetition frequency.

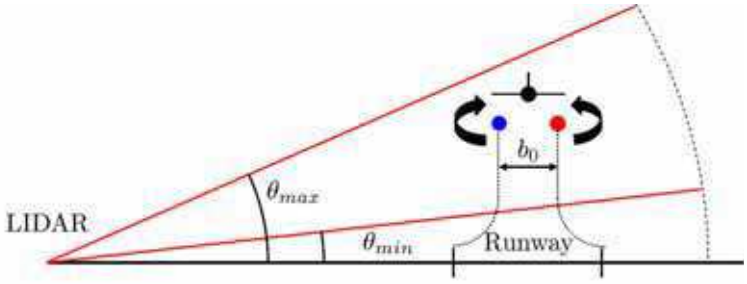

Fig. 3. Lidar scanning pattern on a runway for aircraft wake vortices released close to the ground.

Axial scanning configuration can also be potentially used, especially for onboard LIDAR detection. Nevertheless, the system performance needed are more difficult to attain since the measured radial velocity inside the vortices has a much lower dynamic.

2. Simulation of a Coherent Doppler LIDAR

In heterodyne detection systems, the power of the heterodyne signal at the output of the photodetector is determined by the correlation between the backscattered and the LO fields. This means that any atmospheric phenomena causing the propagating beam to loose its spatial coherence will alter the system efficiency. The main processus involved at low altitude are due to the atmospheric turbulence. The Speckle effect also induces a loss in the signal temporal coherence but it has a limited impact because of its lower time constant. It can therefore be compensated by increasing the level of accumulation during the velocity estimation. The low energy combined with the sensitivity to turbulence increases the need of a precise LIDAR simulation in order to achieve optimal performances. On the one hand, it allows to determine the optimum LASER source and telescope parameters for a given application. Depending on

the constraints of the technology used, it gives the global limits of the system. In the case of fiber LASER sources, the most important parameters are the pulse energy, the pulse duration, the repetition frequency as well as the telescope parameters. On the other hand, it provides simulated signals for the design and validation of velocity estimators and velocity map reconstruction algorithms. The system efficiency in terms of velocity estimation variance and spatial resolution are some of the results obtained from this analysis.

The study of LIDAR performance has largely been investigated using either analytical developments (Frehlich & Kavaya, 1991; Frehlich, 1993) or numerical simulation techniques (Belmonte, 2000; 2003; Frehlich, 2000). The first is somewhat limited to weak fluctutation due to refractive turbulence or the propagation of a untruncated Gaussian beam whereas numerical simulation methods, such as the phase-screen technique has a larger panel of application. The equations describing the LIDAR signal in the temporal domain have first been introduced in Salamitou et al. (1995).

The main originality of the proposed simulation method is the integration of both optical and fluid dynamics numerical methods to take into account the signal coherence loss due to the refractive turbulence, the speckle effect as well as the fine structures of the wake vortex velocity field. It includes also the generation of realistic LIDAR signals in order to develop efficient algorithms for velocity profile estimation and wind velocity map reconstruction. More precisely, the simulation combines the classical signal generation method in the time domain (Salamitou et al., 1995; Van Trees, 2001) with the phase-screen technique used to consider the double-path problem and to compute the heterodyne efficiency and the SNR profiles for a given configuration. To generate the Doppler shifts and induce the signal coherence loss due to wake vortices, a fluid flow simulation is interfaced with the main module. It consists in a large eddy simulation (LES) of incompressible turbulent flow using a high order parallel finite difference code.

In this section, we will describe the time-domain simulation method as well as the phase-screen techniques.

2.1 The heterodyne LIDAR equations

Let assume that the LIDAR system transmits a Gaussian sounding pulse through the atmosphere along a given elevation angle θ. Thus,

$$s_{\mathrm{T}}(t) = \sqrt{2}\Re\left\{\sqrt{E_t}\widetilde{f}(t)e^{j2\pi f_c t}\right\} \tag{6}$$

where E_t [J] is the pulse energy, f_c [Hz] is the intermediate frequency and $\widetilde{f}(t)$ [$\mathrm{s}^{-\frac{1}{2}}$] is the complex envelope of the transmitted pulse defined by

$$\widetilde{f}(t) = \frac{1}{\pi^{1/4}\sigma^{1/2}}\exp\left(-t^2/2\sigma^2\right) \tag{7}$$

where σ is the $1/e$ intensity radius. $\widetilde{f}(t)$ is normalized such that

$$\int_{-\infty}^{\infty}\left|\widetilde{f}(t)\right|^2 dt = 1 \tag{8}$$

Suppose that the atmosphere is divided into layers of thickness dR along the line-of-sight. We transmit a signal s_{T} and examine the signal at time t backscattered from the range interval [R,R+dR]. The signal is the superposition of many reflexions by the aerosol particles contained

in this layer. As the number of aerosol particles illuminated is large, the measured signal is well described by a zero-mean Gaussian random process $\widetilde{b}(t,R)$ and a variance equal to

$$E\left\{|\widetilde{b}(t,R)|^2\right\} = K^2(R)\beta(R)\frac{A_{\mathrm{R}}}{R^2}\eta_{\mathrm{S}}(R,t) \tag{9}$$

where $E\{\}$ represents the statistical average, $K(R)$ is the one-way irradiance extinction taking into account the molecular absorption at the wavelength λ [m], $\beta(R)$ [m^{-1} sr^{-1}] is the aerosol backscatter coefficient, A_{R} [m^2] is the receiver area and η_{S} is the system-antenna efficiency describing the portion of the backscattered field effectively converted to heterodyne signal. The system-antenna efficiency $\eta_{\mathrm{S}}(R)$ term can be computed by using first order analytical equations (Frehlich, 1993) although this approach is limited to weak turbulences and untruncated beams. The contribution of an atmospheric slice at range R to the heterodyne signal at time t is given by

$$\widetilde{s}_{\mathrm{R}}(t,R) = S\sqrt{E_t P_{\mathrm{LO}}}\widetilde{f}(t-2R/c)\widetilde{b}(t,R)\exp(-4\pi v_{\mathrm{R}}(R)t/\lambda)dR \tag{10}$$

where P_{LO} [W] is the local oscillator power, S [A/W] is the detector quantum efficiency and $v_{\mathrm{R}}(R)$ [m/s] is the mean radial velocity of the aerosol particles. The return from the entire atmosphere is the superposition of the returns from the incremental intervals. The complex envelope is

$$\widetilde{s}_{\mathrm{R}}(t) = S\sqrt{E_t P_{\mathrm{LO}}}\int_0^{+\infty}\widetilde{f}(t-2R/c)\widetilde{b}(t-R/c,R)\exp(-4\pi v_{\mathrm{R}}(R)t/\lambda)dR \tag{11}$$

The measured heterodyne current signal [A] at the output of the photodetector is given by

$$i(t) = \sqrt{2}\Re\left\{\widetilde{s}_{\mathrm{R}}(t)e^{j\omega_c t}\right\} + i_{\mathrm{N}}(t) \tag{12}$$

where $i_{\mathrm{N}}(t)$ is noise signal mostly due to the photodetector shot-noise current. It can thus be modeled by an additive Gaussian noise that has a bandpass spectrum and a variance

$$E\left\{|i_{\mathrm{N}}|^2\right\} = 2SeB_w P_{\mathrm{LO}} \tag{13}$$

where e [C/electron] is the electronic charge and B_w [Hz] is the detector bandwidth. The signal-to-noise ratio is then

$$\begin{aligned}\mathrm{SNR}(t) &= \frac{E\left\{|\widetilde{s}_{\mathrm{R}}(t)|^2\right\}}{E\left\{|i_{\mathrm{N}}|^2\right\}} \\ &= \frac{\eta_{\mathrm{Q}}E_t}{\hbar\nu B_w}\int_{-\infty}^{\infty}K^2(R)\beta(R)\frac{A_{\mathrm{R}}}{R^2}|f(t-2R/c)|^2\eta_{\mathrm{S}}(R)dR\end{aligned} \tag{14}$$

The discrete form of the heterodyne signal complexe envelope is given by

$$\widetilde{s}_{\mathrm{R}}(kT_s) = S\sqrt{E_t P_{\mathrm{LO}}}\Delta R\sum_{l=-L_c}^{L_c}\widetilde{f}\left(kT_s - \frac{2}{c}l\Delta R\right)\widetilde{b}(l\Delta R)\exp\left(-4\pi j v_{\mathrm{R}}(l\Delta R)kT_s/\lambda\right) \tag{15}$$

with T_s [s] is the sampling interval and L_c is the summation length chosen to include most of the illuminated aerosol targets. In (Frehlich, 1997), it is proposed to use $L_c = 3.72\sigma(2\Delta R/c)$. In order to completely simulate the LIDAR signal, we need to compute the Doppler shift term as well as the variance of $\widetilde{b}$. The first will be obtained by sampling a simulated wake vortex in ground effect velocity field presented in the section 3. The later will require a complete beam propagation simulation described in the next paragraph.

2.2 Simulation of LASER beam propagation

The phase-screens technique is used here to compute realizations of the system-antenna efficiency η_S intervening in the signal variance. The analysis of its mean value $\langle \eta_S(R) \rangle$ and standard deviation $\langle \eta_S^2(R) \rangle$ are used to optimize the LASER as well as the telescope parameters. This numerical method is particularly suited to simulate the propagation of LASER beams through random media as well as the crossing through the telescope optics.

The scales of turbulence have different effects on the beam depending on their size. Large scales, in the order of the outer scale L_0 of turbulence, cause beam wandering and tilt whereas small ones, with a size close to the inner scale of turbulence l_0 affect the beam coherence. In monostatic configuration, only the latter have a real impact on the system efficiency. A measure of the strength of the turbulence is given by the refractive index structure constant C_n^2. Typical values range from 10^{-18} $m^{-2/3}$ for *weak* turbulence to 10^{-12} $m^{-2/3}$ for *strong* turbulence. It is a constant for horizontal paths and decreases with altitude.

The sounding path is divided into N_r layers of thickness $\Delta R' \gg \Delta R$. A random phase-screen is simulated at each layer. Hence, the LASER beam undergoes phase distortion passing through the screen and is then diffracted within each layer. The propagation of the laser beam $E_T(R, \mathbf{r})$ through layer $[R, R + \Delta R']$ can be written (Banakh et al., 2000) :

$$E(R + \Delta R', \mathbf{s}) = \mathcal{F}^{-1} \left\{ \exp\left(-j\pi\lambda \Delta z' \kappa^2 \right) \mathcal{F} \left[E(R, \mathbf{r}) \exp\left(j\psi(\mathbf{r}) \right) \right] \right\} \tag{16}$$

where $\mathbf{r}$ and $\mathbf{s}$ are the transverse spatial coordinates, $\Psi(\mathbf{r})$ is the random phase screen, κ the spectral coordinate, and $\mathcal{F}$ the Fourier transform operator. The phase-screens are generated using a Von Karman spectrum with a outer scale L_0 of 1 m and a inner scale l_0 of 1cm. Its equation is given by

$$\Phi_n(\kappa) = 0.033 C_n^2 \frac{\exp(-\kappa^2/\kappa_m^2)}{(\kappa^2 + \kappa_0^2)^{11/6}} \qquad , 0 \leq \kappa < \infty \tag{17}$$

where C_n^2 [$m^{-2/3}$] is the refractive-index structure constant, $\kappa_m = 5.92/l_0$ and $\kappa_0 = 1/L_0$. The generation of a phase-screen $\Psi(\mathbf{u})$ from the refractive-index spectrum $\Phi_n(\kappa)$ is given by:

$$\Psi(\mathbf{r}) = 2\pi k^2 \Re \left\{ \mathcal{F} \left[\sqrt{\Phi_n(\kappa)} \xi(\kappa) \right] \right\} \tag{18}$$

where $k = 2\pi/\lambda$ [m^{-1}] is the optival wavenumber and $\xi(\kappa)$ is a zero-mean, unit variance, complex Gaussian random variable. For convenience, the heterodyne mixing is usually computed at the target plane using the backpropagated local oscillator formulation (BPLO). For a general configuration, the emitted as well as the BPLO field must be simulated. The system-antenna efficiency at layer $[R, R + \Delta R']$ can therefore be calculated as follows

$$\eta_S(R) = \frac{\lambda^2 R^2}{A_R} \int_{-\infty}^{\infty} < j_T(R, \mathbf{w}) j_{BPLO}(R, \mathbf{w}) > d\mathbf{w}. \tag{19}$$

where $j_T(R, \mathbf{w})$ and $j_{BPLO}(R, \mathbf{w})$ [m^{-2}] are respectively the irradiance of the normalized transmitted and BPLO fields. The emitted beam is collimated and perfectly Gaussian before passing through the telescope. The LIDAR parameters used for the following simulation are given in Table 2. Due to computational considerations, the PRF has been fixed to 400 Hz which is lower than the PRF provided by a fiber LIDAR (a few kHz).

Simulation parameters	
Laser wavelength	1.55 μm
Pulse energy	150 μJ
Detector bandwidth	50 MHz
Pulse repetition frequency	400 Hz
Intermediate frequency	80 MHz
Sampling frequency	250 MHz
Angular resolution	1.25 mrad
1/e radius of the emitted beam	30mm
Radius of the transmitter aperture	50mm
Aerosol backscattering coefficient	10^{-7} m^{-1} sr^{-1}
Linear extinction coefficient	7.10^{-5} m^{-1}

Table 2. LIDAR parameters used for the simulations

We use a numerical grid for the screen of 512×512 with 2 mm resolution. We simulate a continuous random medium by using 10 phase-screens and the statistics have been obtained by running 400 samples. Fig. 4. gives the SNR as well as the system efficiency at low and medium refractive turbulence level for both monostatic and bistatic configurations. We see on the one hand that an increase of the turbulence level degrades significantly the system performances with range in the bistatic configuration. On the other hand, performance enhancement is observed in the monostatic case which is due to the fact that the emitted and backpropagated beams propagate through the same turbulence. This effect is limited in range and the SNR eventually becomes lower than the one obtained at low C_n^2.

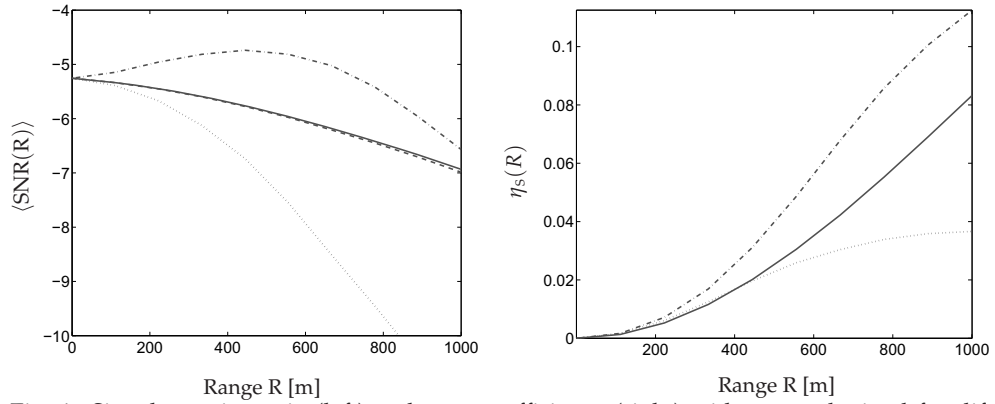

Fig. 4. Signal-to-noise ratio (left) and system efficiency (right) with range obtained for different measurement conditions : free-space (solid); monostatic configuration, $C_n^2 = 10^{-15}$ $m^{-2/3}$ (dash); bistatic configuration, $C_n^2 = 10^{-13}$ $m^{-2/3}$ (dot) and monostatic configuration, $C_n^2 = 10^{-13}$ $m^{-2/3}$ (dash-dot).

3. Simulation of wake vortices in ground effect

In this section, we describe the fluid simulation that have been performed to analyze the detection capability of the heterodyne LIDAR in the presence of wake vortices. Since we consider here a ground-based system, simulating the interaction of wake vortices with the ground is of great importance since it produces secondary vortices.

3.1 Description of the code

The governing equations of the flow considered are the Navier-Stokes equations for incompressible flow, and supplemented by a term which models the effect of the small dissipatives scales of turbulence (not captured by the grid) on the big scales:

$$\nabla \cdot \mathbf{u} = 0 \tag{20}$$

$$\frac{\partial \mathbf{u}}{\partial t} + (\mathbf{u} \cdot \nabla)\,\mathbf{u} = -\nabla P + \nu \nabla^2 \mathbf{u} + \nabla \cdot \boldsymbol{\tau}^M, \tag{21}$$

where P is the reduced pressure, ν is the kinematic viscosity, and $\boldsymbol{\tau}^M$ is the subgrid scale stress tensor model. These equations are solved using a fractional-step method with the *delta* form for the pressure (Lee et al., 2001). This form allows simple boundary conditions for the pressure and the intermediate velocity field. The convective term is integrated using an Adams-Bashforth 2 scheme and the diffusion term using a Crank-Nicolson scheme. The time-stepping scheme reads

$$\begin{aligned} \frac{\mathbf{u}^* - \mathbf{u}^n}{\Delta t} &= -\frac{1}{2}\left(3\mathbf{H}^n - \mathbf{H}^{n-1}\right) - \nabla \phi^n \\ &\quad + \frac{1}{2}\nu \nabla^2 \left(\mathbf{u}^* + \mathbf{u}^n\right) \\ &\quad + \frac{1}{2}\left(3\left(\nabla \cdot \boldsymbol{\tau}^M\right)^n - \left(\nabla \cdot \boldsymbol{\tau}^M\right)^{n-1}\right) \end{aligned} \tag{22}$$

$$\nabla^2 \varphi = \frac{1}{\Delta t} \nabla \cdot \mathbf{u}^* \tag{23}$$

$$\frac{\mathbf{u}^{n+1} - \mathbf{u}^*}{\Delta t} = -\nabla \varphi \tag{24}$$

$$\phi^{n+1} = \phi^n + \varphi, \tag{25}$$

where $\mathbf{H}^n$ is the convective term, $\mathbf{u}^*$ is the intermediate velocity field and ϕ^n is the modified pressure. The model term is integrated explicitly, also using the Adams-Bashforth 2 scheme. The subgrid scale model used here is the WALE regularized variational multiscale model as defined in (Bricteux, 2008). The equations are discretized in space using fourth order finite differences and the scheme of Vasilyev (Vasilyev, 2000) for the discretization of the convective term, which conserves energy on Cartesian stretched meshes and is therefore particularly suited for direct or large-eddy simulations of turbulent flows. The Poisson equation for the pressure is solved using a multigrid solver with a line Gauss-Seidel smoother. The code is implemented to run efficiently in parallel.

3.2 Radial velocity interpolation technique

In order to compute the Doppler term appearing in the equation giving the heterodyne current (Equation 15), the radial velocity in each layer l and for each LOS is mandatory. As the fluid

flow velocity field $(v(y,z),w(y,z))$ issued from the Navier-Stokes simulation is computed on cartesian grid, it is necessary to interpolate the data onto the LIDAR line-of-sight and perform a projection of the velocity vector on the LOS in order to have the radial velocity.
The interpolation scheme selected in this work to interpolate information from a fluid simulation grid grid to the LIDAR measurement points is the M'_4 scheme (Winckelmans, 2004). This technique is widely used in vortex particles methods to redistribute vorticity from a distorded set of particles onto a regular cartesian grid. In this case we perform the inverse operation as we transfer information from a cartesian rectangular grid onto a polar one. This scheme is defined as:

$$\phi^I(\vec{x}) = \sum_{i=0}^{M-1} \sum_{j=0}^{N-1} W(\vec{x} - \vec{x}^S_{ij}) \phi^S_{ij}, \tag{26}$$

where $\vec{x}$ is the lidar sensing location while $\vec{x}^S$ is the location at which the information is computed. The kernel for the M'_4 scheme is defined as:

$$W(x) = \begin{cases} 1 - \frac{5}{2}\left|\frac{x}{h}\right|^2 + \frac{3}{2}\left|\frac{x}{h}\right|^3 & \text{if } \left|\frac{x}{h}\right| \leq 1 \\ \frac{1}{2}\left(2 - \left|\frac{x}{h}\right|\right)^2 \left(1 - \left|\frac{x}{h}\right|\right) & \text{if } 1 < \left|\frac{x}{h}\right| \leq 2 \\ 0 & \text{if } \left|\frac{x}{h}\right| > 2 \end{cases} \tag{27}$$

In Fig. 5, one observes the number of points on the cartesian grid which influence the target point on a LOS. The radial velocity profiles are then obtained by computing the projection of the interpolated velocity profile along the different line-of-sight constituting the scanning pattern.

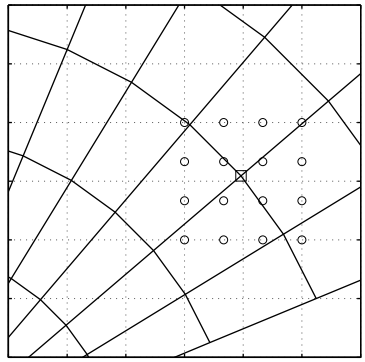

Fig. 5. Interpolation Stencil: the value at a target point (square) located on a given LOS at a given range is obtained by interpolation using the 16 neighbouring points (circles) of the cartesian fluid dynamics simulation grid with a spacing h.

In order to evaluate the estimation error using the fluid simulation velocity field and compare the results with different pulse durations, we have to take into account the radial velocity profile filtering during the measurement process. Hence, the estimated velocity is a filtered

version of the exact radial velocity. The weighting function is the square norm of the transmitted pulse defined in Equation 7. A good approximation of the mean radial velocity estimate is given by (Frehlich, 1997):

$$v_{pulse}(R) = \int_0^\infty v_R(\rho) \left| \widetilde{f}((R-\rho)2/c) \right|^2 d\rho \tag{28}$$

3.3 Results

The results are given with a dimensionless time τ defined as $\tau = tV_0/b_0$, where $V_0 = \Gamma_0/(2\pi b_0)$ is the intial descent velocity of the vortex pair. The flow is evolving in the following way: due to the mutually induced velocity, the vortex pair moves down. The impermeability condition at the wall can be modeled by a mirror vortex pair, resulting in an hyperbolic trajectory. However, as the induced tangential velocity at the wall is nonzero, the no-slip condition is at the origin of the development of boundary layers beneath the vortices. Those are clearly visible in Fig. 6. Starting from the stagnation point on the symmetry plane between the vortices, the pressure gradient forcing the boundary layers is first favorable and then adverse. This leads to their separation, when the primary vortices are close enough to the wall. The detached vortex-sheet then rolls-up and forms two coherent secondary vortices. They induce an upward velocity on the primary vortices and force the latter to rise; this is the rebound phenomenon. At this time, the flow is still essentially two-dimensional. But the secondary vortices are unstable with respect to short-wavelength modes. These perturbations are growing while the secondary vortex is orbiting around the primary vortex, as can be seen in Figs. 6 at time $\tau = 2$. The instability mechanism can be related to the elliptic instability of Widnall. The flow eventually evolves to a fully turbulent vortex system.
The Γ_{5-15} is an important hazard criterion and is defined as the circulation profile average between 5 and 15 meters. Its evolution is reported in Fig. 7. The initial 2-D decay phase is governed by the molecular viscosity and is due to the slow spreading of the core size, it is however negligible in the case of a high *Re* number flow. The fast decay phase starts at $\tau \approx 2.8$ and the final circulation level attained is reduced by 40% compared to the initial one. During the first part of the descent, the trajectoriy follows the inviscid theory. As soon as the boundary layer starts to separate, the rebound occurs and the trajectory is significantly different. One observes the loop trajectory induced by the rebound.
The radial velocity maps in the early case (τ=2.5) and the late case (τ=5) are given Fig. 8.

4. Velocity map reconstruction

Assuming that the LIDAR parameters (pulse energy, duration and PRF) have been optimized for the detection problem, the only constraint subsisting on the signal processing algorithms is to guarantee the best spatial resolution while keeping the radial velocity estimation variance as low as possible. This constraint is related to the use of accumulation methods to compensate the low SNR. As circulation estimation method are usually based on a model-fitting method, a poor spatial resolution inside vortices will induce inherently a higher estimation variance on the vortex circulation. The goal of this section is therefore to compare the efficiency of periodogram-based and correlogram-based accumulation methods in terms of spatial resolution in the vicinity of the wake vortex.

4.1 Radial velocity estimation

Each time a pulse is sent, along a particular line-of-sight (LOS) of given elevation angle defined by the current position of the telescope, a signal $s(nT_s)$ is measured where T_s is the

sampling period. In order to evaluate the velocity profile along this LOS, we estimate the energy spectral density of $s(nT_s)$ at each position of a sliding window of N time samples. The observation time is then $T_{obs} = NT_s$ which corresponds to a range gate size $\Delta p = T_{obs}c/2$. The time offset of the pth window is t_p and the spatial offset is then $R_p = t_p c/2$. A direct spectral estimate is the periodogram defined by

$$\widehat{P}_s(k\Delta f) = \frac{1}{N}\left|\sum_{n=0}^{N-1} h(nT_s)s(t_p + nT_s)\exp\left(-2\pi ikn/N\right)\right|^2 \tag{29}$$

If no spectral interpolation is performed, the frequency resolution is $\Delta f = F_s/N$. An estimate of mean velocity, $\hat{v}_{\mathrm{R}}$, is given by evaluating

$$\hat{v}_{\mathrm{R}} = \frac{\lambda}{2}\left(f_c - \frac{F_s}{N}\mathrm{argmax}_k\left\{\hat{P}_s[k]\right\}\right) \tag{30}$$

where f_c [Hz] is the intermediate frequency and h is the signal weighting function (usually Gaussian). A parametric spectral estimation method is also possible usually leading to better velocity estimates at moderate noise level. The signal $s(nT_s)$ at a given position of the window can be modeled by a p-order autoregressive model, noted AR(p). The difference equation describing this model is

$$x(n) = -\sum_{k=1}^{p} a_k x(n-k) + w(n) \tag{31}$$

where $\{a_k\}$ are the parameters of the model and $w(n)$ is the input sequence of the model, i.e. a white noise with zero mean and variance σ^2. The corresponding power spectrum estimate can then be expressed in term of the AR coefficients

$$\widehat{P}_s^{\mathrm{AR}}(k\Delta f) \equiv \frac{\sigma^2}{|A(k)|^2} = \frac{\sigma^2}{\left|1 + \sum_{k=1}^{p} a_k exp(-j2\pi kf)\right|^2} \tag{32}$$

The $\{a_k\}$ parameters are calculated in this work by the Yule-Walker method and the Levinson-Durbin algorithm for which an estimation of the signal correlogram is needed. The spectrum of an AR(p) process has at most p poles, i.e. frequencies minimizing $A(k)$. Those models are good candidates to represent sharp spectral peaks but not spectral valleys since they have no zeros. However, if p is chosen large enough, AR techniques can approximate adequately any kind of spectral shapes. The model parameters estimation technique is described in (Proakis, 1965). The velocity estimate is then computed using Equation 30. We use a fixed model order of p=16.

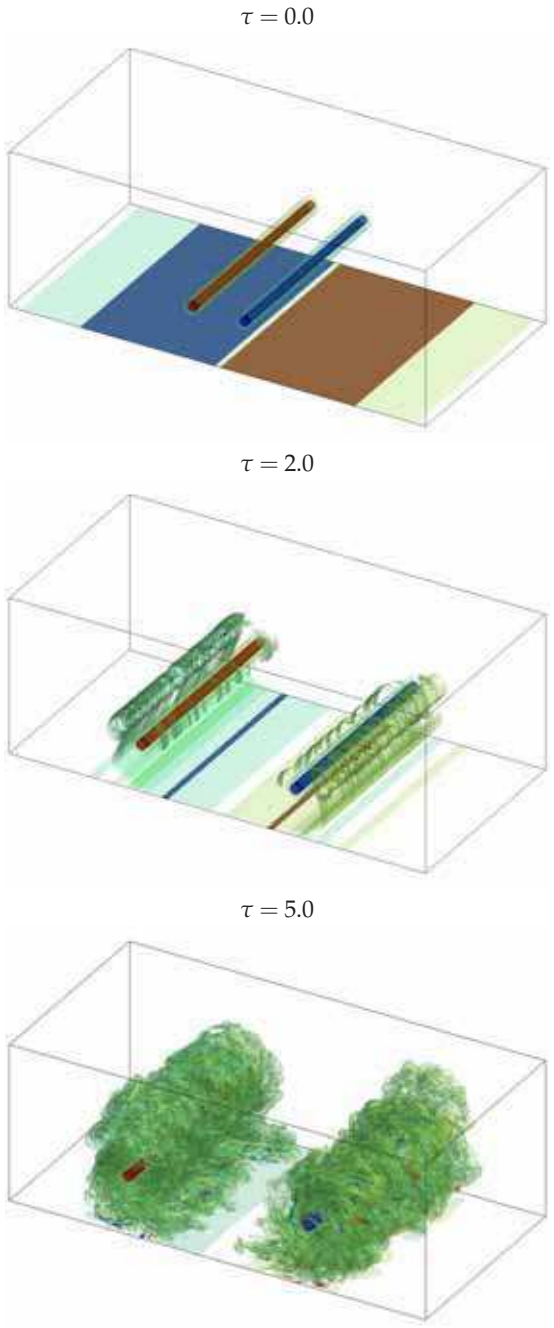

Fig. 6. Visualization of the flow field using isosurfaces of $\|\vec{\nabla} \times \mathbf{u}\| b_0^2/\Gamma_0 = 1$ and 10.

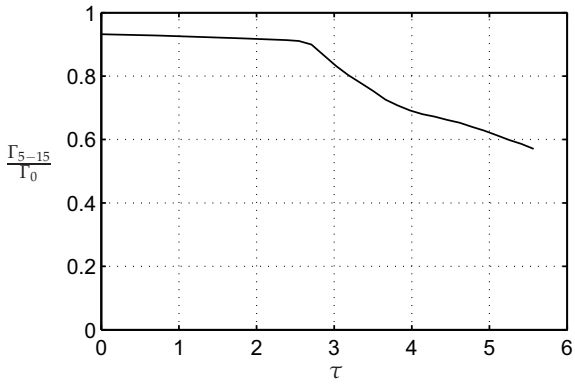

Fig. 7. Temporal evolution of the Γ_{5-15}.

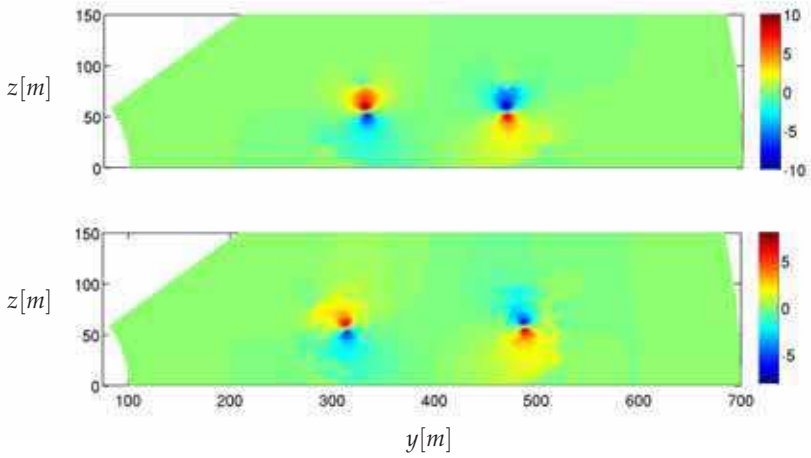

Fig. 8. Radial velocity maps v_R [m/s] of the wake vortices in ground effect at dimensionless time τ=2.5 (top, early case) and τ=5 (bottom, late case).

4.2 Accumulation strategies

Due to the low pulse energy provided by fiber-based LIDAR , the velocity estimates obtained from a single spectral density estimate are rather poor. In order to reduce the estimation variance, two different kinds of accumulation strategies are used: a periodogram accumulation and a correlogram accumulation (Rye & Hardesty, 1993). We apply these concepts here in the case of 2D velocity map reconstruction in order to compare their performances when wake vortices are present in the sensing volume.

Each signal window is defined by a vector $\mathbf{k}$ with polar coordinates $R = \frac{c}{2}(t_p + N_w T_s/2)$ [m] and θ [rad] being the elevation angle defining the line-of-sight. The processing vector set $\{\mathbf{k}\}$ is denoted $\mathcal{K}$. We define I_k as either the periodogram or the correlogram computed from the signal window $s_\theta(t_p + nTs)$ with $n = 0,\ldots,N_w - 1$. The main idea is to compute

an averaged estimate I_p at a set of spatial positions $\mathbf{p}$ using the estimations I_k included in a circular region-of-interest $\mathcal{C}$ around this point $\mathbf{p}$. The accumulation algorithm is given in Table 3. Once the radial velocity has been estimated at each point $\mathbf{p}$, the estimation error is computed by the mean square error between the estimated radial velocity $\hat{v}_{\mathrm{R}}$ and the exact filtered radial velocity $v_{pulse}(\mathbf{p})$:

$$\mathrm{MSE}(\mathbf{p}) = |\hat{v_{\mathrm{R}}}(\mathbf{p}) - v_{pulse}(\mathbf{p})|^2 \tag{33}$$

4.3 Results

The accumulation level, defined as the number of estimates I_k used for one radial velocity estimation $\hat{v}_{\mathrm{R}}$, is given at Fig. 9. In order to have the same spatial resolution at each point $\mathbf{p}$ a constant radius ρ with distance R have been chosen. As the measurement is performed on a polar grid, the accumulation level decreases with R. The vortex pair is situated around 400 m from the LIDAR. At this distance, a radius ρ of 1, 2 and 4 m corresponds to an accumulation level per velocity estimate of respectively 20, 60 and 120 k-points. For a given radius, the accumulation level depends also on the pulse repetition frequency.

Using a fixed radius implies the variance of the spectral density estimates to increase with range R due to variable accumulation level and SNR fluctuation. However, it is more interesting to choose a range-dependent radius by determining an optimal trade-off between spatial resolution (accumulation level) and velocity resolution (spectral density estimate variance). Fig. 10 gives the spatial variation of the MSE compared with the exact radial velocity field. We observe that the estimation error increases inside the vortex where the velocity gradients along the propagation direction are the most important. High velocity gradients decrease the temporal coherence of the signal and consequently induce a broadening of the signal spectrum with a decrease of its maximum value. Moreover, the accumulation process combined with the *argmax* estimation tends to promote narrow spectra computed outside the vortex. This effect must be take into account since it distorts the retrieved vortex shape and increases the error made on subsequent model-fitting algorithms dedicated to circulation estimation.

Accumulation algorithm :

$\forall \mathbf{k} \in \mathcal{K}$,
  Estimates I_k from $s_\theta(t_p + nTs), n = 0, \ldots, N_w - 1$
$\forall \mathbf{p} \in \mathcal{R}$,
  Define $\mathcal{C}$ with radius $\rho = \rho(R)$.
  $n \leftarrow 0$;
  $\forall \mathbf{k} \in \mathcal{K} \mid \mathrm{dist}(\mathbf{p}, \mathbf{k}) \leq \rho(R)$
    $I_p \leftarrow (nI_p + I_k)\frac{1}{1+n}$;
    $n \leftarrow n + 1$;
  Estimate spectral density from I_p
  Estimate $\hat{v}(\mathbf{p})$

Table 3. Accumulation algorithm. I_k is either the periodogram or the correlogram of the signal.

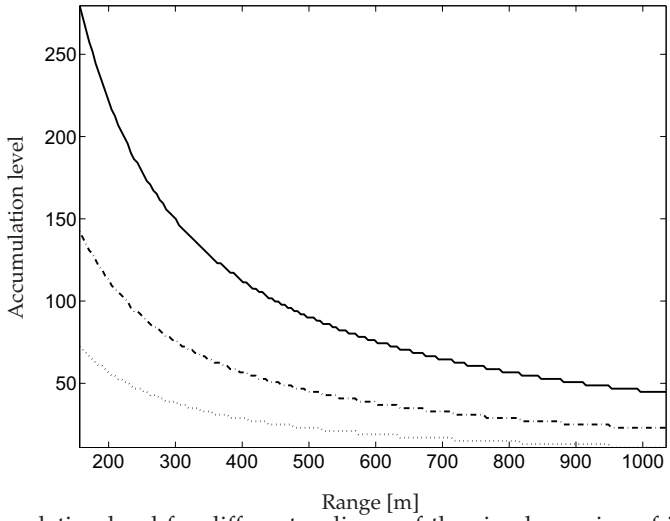

Fig. 9. Accumulation level for different radius ρ of the circular region-of-interest: $\rho = 1$ m (dot), $\rho = 2$ m (dash-dot) and $\rho = 4$ m (solid).

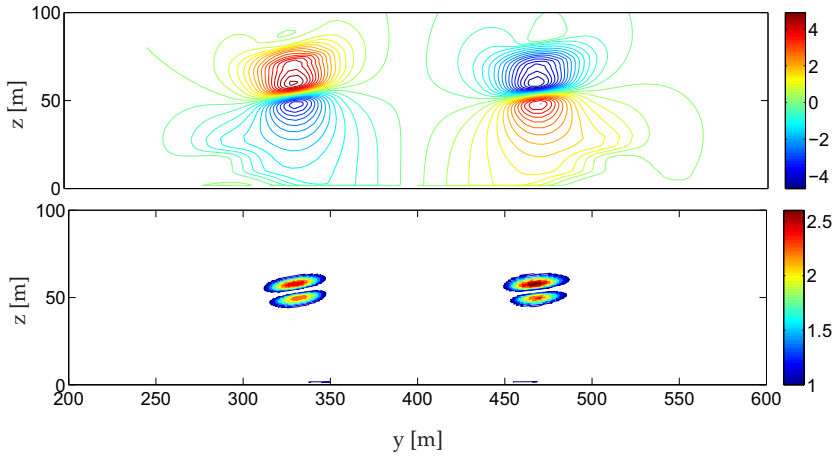

Fig. 10. Influence of the accumulation process on the estimation error. Radial velocity map v_R (top) and standard deviation σ_v [m/s] (bottom).

The processing results obtained for wake vortices in the late case with a pulse duration of 400 ns and a refractive index $C_n^2 = 10^{-15}$ m$^{-2/3}$ is given Fig. 11. The window length has been fixed to $N = 64$ samples which gives a range gate of 38.4 m. Comparing this results with Fig. 8

(bottom) allows to illustrate the radial velocity filtering inherent to wind measurement with a pulsed LASER .
Fig. 12. shows the standard deviation of the radial velocity estimates averaged over all the line-of sight $\langle \sigma_v \rangle$ for different values of the pulse energy E_t. It has been obtained in the early case (young vortices) with a pulse duration of 200 ns and strong turbulence $C_n^2 = 10^{-13}$ m$^{-2/3}$. The algorithm used is the correlogram-accumulation method. We see that reducing the pulse

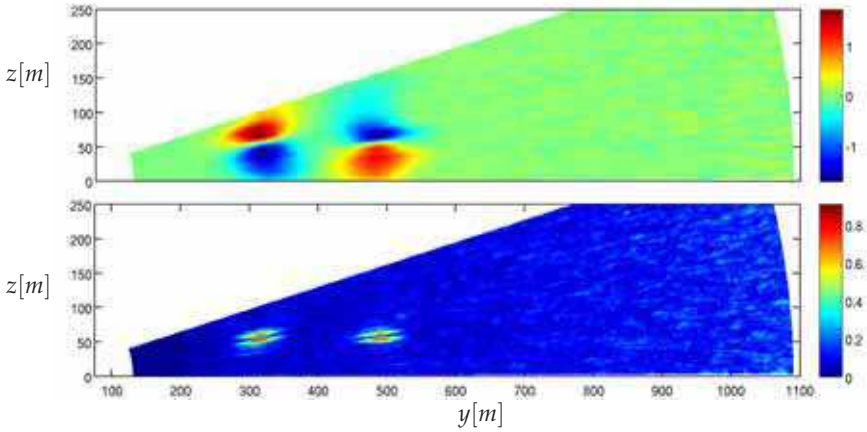

Fig. 11. Signal processing results: estimation of the radial velocity map (top) and MSE (bottom) obtained in the late case. The pulse duration is 400 ns and the refractive index is $C_n^2 = 10^{-15}$ m$^{-2/3}$.

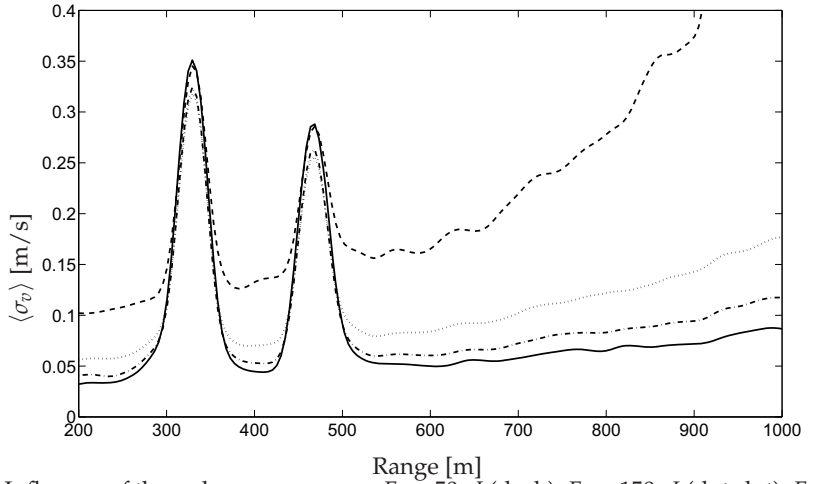

Fig. 12. Influence of the pulse energy on σ_v. $E_t = 50\mu J$ (dash); $E_t = 150\mu J$ (dot-dot); $E_t = 300\mu J$ (dash-dot) and $Et = 600\mu J$ (solid) obtained with the correlogram accumulation method ($\rho = 2$ m). The pulse duration is 200 ns. The refractive index is $C_n^2 = 10^{-13}$ m$^{-2/3}$.

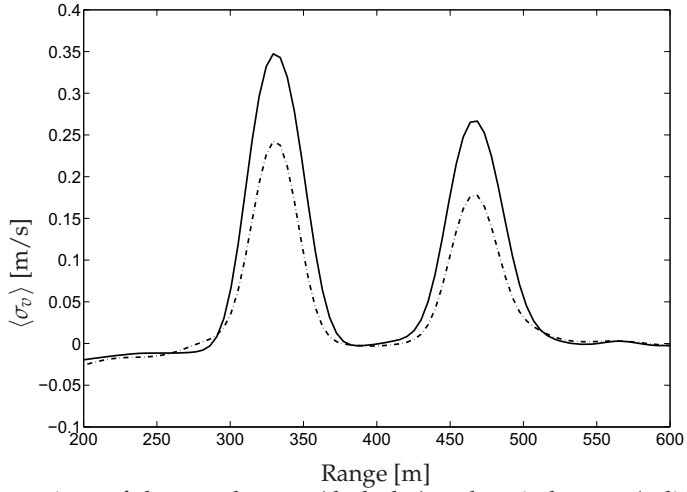

Fig. 13. Comparison of the correlogram (dash-dot) and periodogram (solid) accumulation methods at 200 ns for young vortices. The accumulation radius is 2 m.

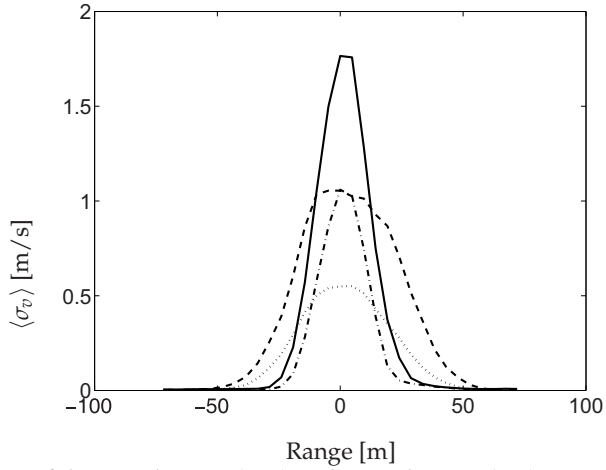

Fig. 14. Comparison of the correlogram (CA) and periodogram (PA) accumulation methods: PA, 200ns (solid); CA, 200ns (dash-dot); PA, 400ns (dash); CA, 400ns (dot). The refractive index is $C_n^2 = 10^{-15}$ m$^{-2/3}$. The range is given such that $R = 0$ m at the vortex center.

energy has no influence inside vortices whereas it monotically increases with range. It must be noted that, as pointed by Equation 14, for the same telescope configuration and beam sizes, the SNR is identical provided that we keep the ratio $\beta E_t / B_w$ constant. Hence, decreasing the pulse energy by a factor of 2 for example, gives the same estimation variance than decreasing by the same factor the aerosol particles density. The comparison between the two accumulation strategies are given at Fig. 13 and Fig. 14. The standard deviation of the velocity

estimate are given after having removed the averaged evolution due to SNR variation. The correlogram accumulation gives better results inside the vortices at 200 ns and 400 ns. The error profiles are both narrower (spatial resolution) and smaller (velocity resolution) which induces better results for subsequent circulation estimation algorithm based on model-fitting as described in (Brousmiche et al., 2009).

5. Conclusions

The main originality of the simulation framework proposed here is to link numerical simulation techniques belonging to optical propation and fluid dynamics theory in order to assess the feasibility of wake vortex detection using a fiber-based heterodyne Doppler LIDAR. Moreover, the generation of realistic LIDAR signals with temporal decorrelation due to Speckle and beam propagation through wake vortices allows to develop efficient velocity estimation algorithms. Two accumulation-based algorithms have been tested and their performances in the vicinity of the vortices have been compared. It results that the correlogram accumulation method gives the best compromise between velocity and spatial resolution than the periodogram accumulation method generally used in such application. This feature is important since the main objective is the estimation of wake vortex circulation in order to evaluate their strength (usually by means of model-based algorithms).
Our analysis has principally focused on the detection of wake vortices interacting with the ground. An interesting study would be to consider cross wind as it appears in real atmospheric conditions. The transmission of radial velocity estimation errors on the estimation of vortex strength would also be considered.

6. Acknowledgements

The fluid and LIDAR simulations were done using the facilities of the Calcul Intensif et Stockage de Masse (CISM) on the UCL Lemaître cluster funded by Fond National de Recherche Scientifique (FNRS) under a FRFC Project and by UCL (Fonds Spéciaux de Recherche). Results were obtained in the framework of the LASEF project funded by the Région Wallonne of Belgium.

7. References

Banakh, V. A., Smalikho, I. N. & Werner, C. (2000). Numerical simulation of the effect of refractive turbulence on coherent lidar return statistics in the atmosphere, *Applied Optics*, **Vol.** 39(No. 30): 5403-5414.

Belmonte, A. & Rye, B. J. (2000). Heterodyne lidar returns in the turbulent atmosphere: performance evaluation of simulated systems, *Applied Optics*, **Vol.** 39(No. 15): 2401-2411.

Belmonte, A. (2003). Analyzing the efficiency of a practical heterodyne lidar in the turbulent atmosphere: telescope parameters, *Optics express*, **Vol.** 11(No. 17): 2041-2046.

Bricteux, L. (2008). A new multiscale model with proper behaviour in both vortex flows and wall bounded flows, *Direct and Large-Eddy Simulation VII book, ERCOFTAC Series*, Springer.

Brousmiche, S., Bricteux, L., Sobieski, P., Winckelmans, G., Macq, B. & Craeye, C. (2009). Parameters Estimation of Wake Vortices in Ground Effect, *Proceedings of the 15th Coherent Laser Radar Conference*, Toulouse, pp. 149-152.

Frehlich, R. G. and Kavaya, M. G. (1991). Coherent laser radar performance for general atmospheric refractive turbulence, *Applied Optics*, **Vol.** 30(No. 36): 5325-5351.

Frehlich, R. G. (1993). Effect of refractive turbulence on coherent laser radar, *Applied Optics*, **Vol.** 32(No. 12): 2122-2139.

Frehlich, R. G. (1997). Effect of Wind Turbulence on Coherent Doppler Lidar Performance, *Journal of Atmospheric and Oceanic Technology*, **Vol.** 14.

Frehlich, R. G. (2000). Simulation of laser propagation in a turbulent atmosphere, *Applied Optics*, **Vol.** 39(No. 3).

Gerz, T., Holzapfel, F. & Darracq D. (2001). Aircraft wake vortices: a position paper, Wakenet, the european thematic network on wake vortex position paper.

Levin, M. J. (1965). Power Spectrum Parameter Estimation, *IEEE Trans. on Information theory*, **Vol.** IT-11: pp 100-107

Lee, M. J., Oh, B. D. & Kim, Y. B. (2001). Canonical Fractional-Step Methods and Consistent Boundary Conditions for the Incompressible Navier Stokes Equations, *J. Comp. Phys.*, **Vol.** 168: 73-100.

Martin, J. M. & Flaté, S. M. (1990). Simulation of point-source scintillation through three-dimensional random media, *J. Opt. Soc. Am. A*, **Vol.** 7(No. 5): 838-847.

Prandtl, L. & Tietjens, O.G (1957). *Fundamentals of hydro- and aero-mechanics*, Dover publ.

Proakis, J. G. (1965). *Digital Signal Processing : Principles, Algorithms and Applications*, Prentice Hall.

Rye, B. J. & Hardesty, R. M. (1993). Discrete Spectral Peak Estimation in Incoherent Backscatter Heterodyne Lidar. I: Spectral Accumulation and the Cramer-Rao Lower Bound, *IEEE Trans. on Geoscience and Remote Sensing*, **Vol.** 31(No. 1): 16-27.

Rye, B. J. & Hardesty, R. M. (1993). Discrete Spectral Peak Estimation in Incoherent Backscatter Heterodyne Lidar. II: Correlogram Accumulation, *IEEE Trans. on Geoscience and Remote Sensing*, **Vol.** 31(No. 1): 28-35 .

Salamitou, P., Dabbas, A. & Flamant, P. (1995). Simulation in the time domain for heterodyne coherent laser radar, *Applied Optics*, **Vol.** 34(No. 3): 499-506.

Van Trees, H. (2001). *Detection, Estimation and Modulation Theory. Radar-sonar Processing and Gaussian Signals in Noise*, Wiley, 2001

Vasilyev, O. V. (2000). High order finite difference schemes on non-uniform meshes with good conservation properties, *J. Comp. Phys.*, **Vol.** 157(No. 2): 746-761.

Winckelmans, G. S. (2004). Chapter 5: Vortex Methods, *Encyclopedia of Computational Mechanics*, Erwin Stein, René de Borst, Thomas J.R. Hughes (Eds), John Wiley & Sons.

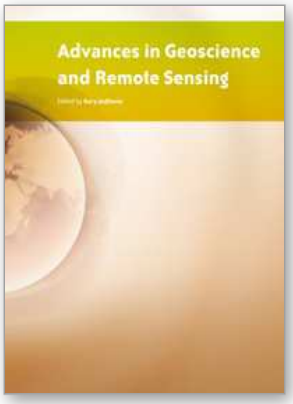

Advances in Geoscience and Remote Sensing

Edited by Gary Jedlovec

ISBN 978-953-307-005-6

Hard cover, 742 pages

Publisher InTech

Published online 01, October, 2009

Published in print edition October, 2009

Remote sensing is the acquisition of information of an object or phenomenon, by the use of either recording or real-time sensing device(s), that is not in physical or intimate contact with the object (such as by way of aircraft, spacecraft, satellite, buoy, or ship). In practice, remote sensing is the stand-off collection through the use of a variety of devices for gathering information on a given object or area. Human existence is dependent on our ability to understand, utilize, manage and maintain the environment we live in - Geoscience is the science that seeks to achieve these goals. This book is a collection of contributions from world-class scientists, engineers and educators engaged in the fields of geoscience and remote sensing.

How to reference

In order to correctly reference this scholarly work, feel free to copy and paste the following:

S. Brousmiche, L. Bricteux, G. Winckelmans, B. Macq and P. Sobieski (2009). Modeling of Wake-Vortex Detection by a Ground-based Fiber LIDAR System, Advances in Geoscience and Remote Sensing, Gary Jedlovec (Ed.), ISBN: 978-953-307-005-6, InTech, Available from: http://www.intechopen.com/books/advances-in-geoscience-and-remote-sensing/modeling-of-wake-vortex-detection-by-a-ground-based-fiber-lidar-system

INTECH

open science | open minds

InTech Europe

University Campus STeP Ri
Slavka Krautzeka 83/A
51000 Rijeka, Croatia
Phone: +385 (51) 770 447
Fax: +385 (51) 686 166
www.intechopen.com

InTech China

Unit 405, Office Block, Hotel Equatorial Shanghai
No.65, Yan An Road (West), Shanghai, 200040, China
中国上海市延安西路65号上海国际贵都大饭店办公楼405单元
Phone: +86-21-62489820
Fax: +86-21-62489821

© 2009 The Author(s). Licensee IntechOpen. This chapter is distributed under the terms of the Creative Commons Attribution-NonCommercial-ShareAlike-3.0 License, which permits use, distribution and reproduction for non-commercial purposes, provided the original is properly cited and derivative works building on this content are distributed under the same license.